

Kepler and the Behemoth: Three Mini-Neptunes in a 40 Million Year Old Association

L. G. BOUMA,^{1,*} R. KERR,² J. L. CURTIS,^{3,4} H. ISAACSON,⁵ L. A. HILLENBRAND,¹ A. W. HOWARD,¹ A. L. KRAUS,² A. BIERYLA,⁶
D. W. LATHAM,⁶ E. A. PETIGURA,⁷ AND D. HUBER⁸

¹*Cahill Center for Astrophysics, California Institute of Technology, Pasadena, CA 91125, USA*

²*Department of Astronomy, The University of Texas at Austin, Austin, TX 78712, USA*

³*Department of Astronomy, Columbia University, 550 West 120th Street, New York, NY 10027, USA*

⁴*Department of Astrophysics, American Museum of Natural History, New York, NY 10024, USA*

⁵*Astronomy Department, University of California, Berkeley, CA 94720, USA*

⁶*Center for Astrophysics | Harvard & Smithsonian, 60 Garden St, Cambridge, MA 02138, USA*

⁷*Department of Physics & Astronomy, University of California Los Angeles, Los Angeles, CA 90095, USA*

⁸*Institute for Astronomy, University of Hawaii, 2680 Woodlawn Drive, Honolulu, HI 96822, USA*

(Received April 10, 2022; Revised —; Accepted —)

ABSTRACT

Stellar positions and velocities from Gaia are yielding a refined view of open cluster dispersal. Here we present an analysis of a group stars spanning Cepheus ($l = 100^\circ$) to Hercules ($l = 40^\circ$), hereafter the Cep-Her complex. The group includes four Kepler Objects of Interest: Kepler-1643 b ($R_p = 2.32 \pm 0.14 R_\oplus$, $P = 5.3$ days), KOI-7368 b ($R_p = 2.22 \pm 0.12 R_\oplus$, $P = 6.8$ days), KOI-7913 Ab ($R_p = 2.34 \pm 0.18 R_\oplus$, $P = 24.2$ days), and Kepler-1627 Ab ($R_p = 3.85 \pm 0.11 R_\oplus$, $P = 7.2$ days). The latter Neptune-sized planet is in a component of the Cep-Her complex called the δ Lyr cluster (Bouma et al. 2022). Here we focus on the former three systems, which are in other regions of the association. Based on kinematic evidence from Gaia, stellar rotation periods from TESS, and spectroscopy, these three systems are also ≈ 40 million years (Myr) old. More specifically, we find that Kepler-1643 is 46^{+9}_{-7} Myr old, based on its membership in a dense sub-cluster of the complex called RSG-5. KOI-7368 and KOI-7913 are 36^{+10}_{-8} Myr old, and are in a diffuse region that we call CH-2. Based on the transit shapes and high resolution imaging, all three objects are most likely planets, with false positive probabilities of 6×10^{-9} , 4×10^{-3} , and 1×10^{-4} for Kepler-1643, KOI-7368, and KOI-7913 respectively. These planets empirically demonstrate that mini-Neptunes with sizes of ≈ 2 Earth radii exist at ages of ≈ 40 million years.

Keywords: exoplanet evolution (491), open star clusters (1160), stellar ages (1581)

1. INTRODUCTION

The discovery and characterization of transiting planets younger than a billion years is a major frontier in current exoplanet research. The reason is that the properties of young planets provide benchmarks for studies of planetary evolution. For instance, there are the questions of when hot Jupiters arrive on their close-in orbits (Dawson & Johnson 2018), how the sizes of planets with massive gaseous envelopes evolve (Rizzuto et al. 2020), when and if close-in multiplanet systems fall out of resonance (Arevalo et al. 2022; Goldberg & Batygin 2022), and whether and how

mass-loss explains the radius valley (Lopez et al. 2012; Owen & Wu 2013; Fulton et al. 2017; Ginzburg et al. 2018; Lee & Connors 2021).

The discovery of a young planet requires two claims to be fulfilled: the planet must exist, and its age must be secured. Spaced-based photometry from K2 and TESS has yielded a number of young planets for which the planetary evidence comes from transits, and the age is based on either cluster membership (Mann et al. 2017; David et al. 2019; Newton et al. 2019; Bouma et al. 2020; Nardiello et al. 2020) or else on correlates of youth such as stellar rotation, photospheric lithium content, x-ray activity, or emission line strength (Zhou et al. 2021; Hedges et al. 2021).

In this work, we leverage recent analyses of the Gaia data, which have greatly expanded our knowledge of stellar groups (e.g., Cantat-Gaudin et al. 2018; Kounkel & Covey 2019; Kerr et al. 2021). To date these analyses have mostly clus-

Corresponding author: L. G. Bouma
luke@astro.caltech.edu

* 51 Pegasi b Fellow

tered on the stellar positions and 2-D velocities measured by Gaia. One important result is the discovery of diffuse streams and tidal tails comparable in stellar mass to the previously known cores of nearby open clusters (Meingast et al. 2019; Meingast et al. 2021; Gagné et al. 2021). Even though these streams can be spread out over tens to hundreds of parsecs, their velocity dispersions can remain coherent at the $\sim 1 \text{ km s}^{-1}$ level. They can also be much larger: as an extreme example, internal dynamics and projection effects in the Hyades drive stars in the tidal tails span up to $\pm 40 \text{ km s}^{-1}$ in relative velocity when projected against the cluster center (Jerabkova et al. 2021). The stars in such diffuse regions can be verified to be the same age as the core members (*i.e.*, coeval) through analyses of color-absolute magnitude diagrams (Kounkel & Covey 2019), stellar rotation periods (Curtis et al. 2019; Bouma et al. 2021), and chemical abundances (Hawkins et al. 2020). While there are many implications for our understanding of star formation and cluster evolution (Dinnbier & Kroupa 2020), a separate consequence is that we now know the ages of many more stars, including previously known planet hosts.

The prime Kepler mission (Borucki et al. 2010) found most of the currently known transiting exoplanets, and it was conducted before Gaia. It is therefore sensible to revisit the Kepler field, given our new knowledge of the stellar ages.

In this work, we expand on our previous study of a 38_{-6}^{+7} Myr old Neptune-sized planet in the Kepler field (Kepler-1627 Ab; Bouma et al. 2022). The age of this planet was derived based on its host star’s membership in the δ Lyr cluster. Our analysis of the cluster focused on the immediate spatial and kinematic vicinity of Kepler-1627 A in order to secure the planet’s age. However it became clear that the δ Lyr cluster seems to also be part of a much larger group of similarly aged stars. This group, which is at a distance of ~ 330 pc from the Sun, appears to span Cepheus to Hercules (galactic longitudes, l , between 40° and 100°), at galactic latitudes roughly between 0° and 20° . We therefore refer to it as the Cep-Her complex. It exhibits significant sub-structure over its ≈ 250 parsec length, and a detailed analysis of its memberships, kinematics, and possible origin is currently being prepared by R. Kerr and collaborators.

Here, our focus is on the intersection of the Cep-Her complex with the Kepler field. Cross-matching the full set of candidate Cep-Her members against known Kepler Objects of Interest (KOIs) (Thompson et al. 2018) yielded four candidate cluster members: Kepler-1627, Kepler-1643, KOI-7368, and KOI-7913. Given our previous analysis of Kepler-1627, we will mostly focus on the latter three. After analyzing the relevant properties of Cep-Her (Section 2), we derive the stellar properties (Section 3) and validate the planetary nature of each system using a combination of the Kepler photometry and high-resolution imaging (Section 4). We conclude with

a few caveats, and discuss implications for the size-evolution of close-in mini-Neptunes (Section 5).

2. THE CEP-HER COMPLEX

2.1. Previous Related Work

Our focus is on a region of the Galaxy approximately 200 to 500 pc from the Sun, above the galactic plane, and spanning galactic longitudes of roughly 40° to 100° degrees. Two rich clusters in this region are the δ Lyr cluster (Stephenson 1959) and RSG-5 (Röser et al. 2016). Each of these clusters was known before Gaia. They have reported ages between 30 and 60 Myr. Early empirical evidence that these two clusters could be part of a large and more diffuse population was apparent in the Gaia-based photometric analysis of pre-main-sequence stars by Zari et al. (2018, see their Figures 11 and 13). Further kinematic connections and complexity were highlighted by Kounkel & Covey (2019), who included these previously known groups in the larger structures dubbed “Theia 73” and “Theia 96”¹. The connection made by Kounkel & Covey (2019) between the previously known open clusters and the other groups in the region was made as part of an unsupervised clustering analysis of the Gaia DR2 positions and tangential velocities with a subsequent manual “stitching” step. Their results support the idea that there is an overdensity of 30 to 60 Myr old stars in this region of the Galaxy. Kerr et al. (2021), in a volume-limited analysis of the Gaia DR2 point-source catalog out to one third of a kiloparsec, identified three of the nearest sub-populations, dubbed “Cepheus-Cygnus”, “Lyra”, and “Cerberus”. Kerr et al. (2021) reported ages for each of these subgroups between 30 and 35 Myr.

2.2. Member Selection

The possibility that the δ Lyr cluster, RSG-5, and the sub-populations identified by Kerr et al. (2021) share a common origin has yet to be fully substantiated, and is the subject of the upcoming study by R. Kerr and collaborators. Our primary interest in the region stems from the fact that a portion of it was observed by Kepler (Figure 1, top panel). To further explore the population of stars that were observed, we select candidate Cep-Her members through four steps, the first three being identical to those described in Section 3 of Kerr et al. (2021). We briefly summarize them here.

The first step is to select stars that are photometrically distinct from the field star population based on Gaia EDR3 magnitudes $\{G, G_{\text{RP}}, G_{\text{BP}}\}$, parallaxes and auxiliary reddening estimates (Lallement et al. 2019). This step yielded 1097 stars with high-quality photometry and astrometry. These stars are either pre-main-sequence K and M dwarfs due

¹ See their visualization online at <http://mkounkel.com/mw3d/mw2d.html> (accessed 15 March 2022)

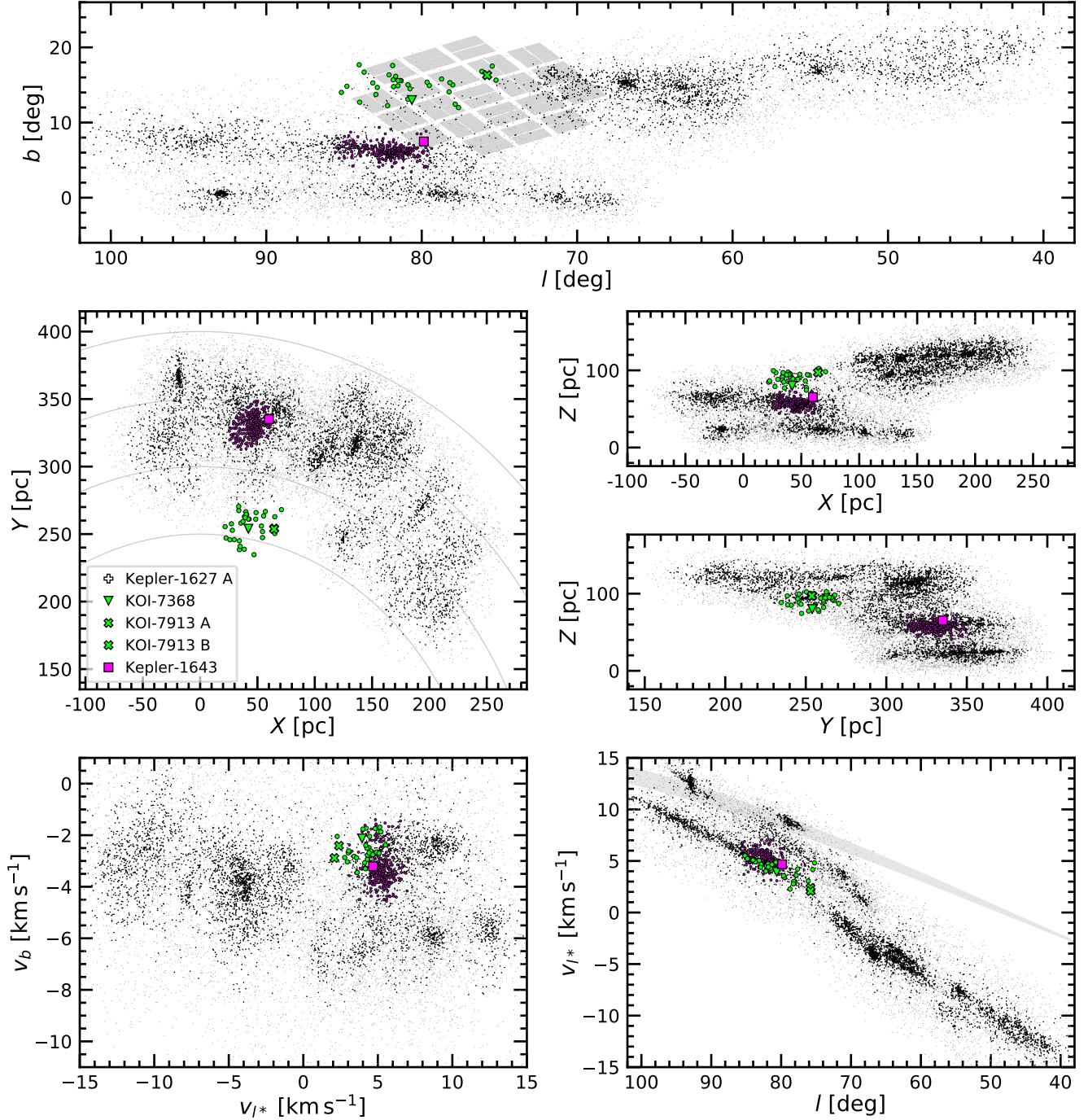


Figure 1. Positions and velocities of candidate members of the Cep-Her complex. *Top row:* On-sky positions in galactic coordinates. Black points are stars for which group membership is more secure than for gray points. Kepler-1627 is in the outskirts of the δ Lyr cluster (Bouma et al. 2022), which is centered at $\{l, b\} \approx \{66^\circ, 12^\circ\}$. *Middle row:* Galactic positions. The Sun is at $\{X, Y, Z\} = \{0, 0, 20.8\}$ pc; lines of constant heliocentric distance are shown between 250 and 400 pc, spaced by 50 pc. *Bottom row:* Galactic tangential velocities (left) and galactic longitudinal velocity versus galactic longitude (right). The gray band in the lower-right shows the $\pm 1\text{-}\sigma$ projection of the Solar velocity with respect to the local standard of rest. There is a strong spatial and kinematic overlap between Kepler-1643 and RSG-5 (magenta). The local population of candidate young stars around KOI-7368 and KOI-7913 is more diffuse – we call this region “CH-2” (lime-green). The selection method for the black, gray, purple, and green points is described in Section 2.2.

to their long contraction timescales, or massive stars near the zero-age main sequence due to their rapid evolutionary timescales.

The second step is to perform an unsupervised HDB-Scan clustering on the photometrically selected population (Campello et al. 2015; McInnes et al. 2017). The parameters we use in the clustering are $\{X, Y, Z, cv_b, cv_{l^*}\}$, where c is the size-velocity corrective factor, which is taken as $c = 6 \text{ pc/km s}^{-1}$ to ensure that the spatial and velocity scales have identical standard deviations. Positions are computed assuming the `astropy v4.0` coordinate standard (Astropy Collaboration et al. 2018), which places the Sun 8122 pc from the galactic center, and assumes the solar velocity with respect to the local standard of rest from Schönrich et al. (2010). As input parameters to HDBScan, we set the minimum ϵ threshold past which clusters cannot be fragmented as 25 pc in physical space, and $c \text{ km s}^{-1}$ in velocity. The minimum cluster size N is set to 10, as is k , the parameter used to define the “core distance” density metric.

This unsupervised clustering in our case yielded 8 distinct groups. These groups are then used as the “seed” populations for the third step, which is to search for objects at least as close to the 10th nearest HDBSCAN-identified member in space-velocity coordinates. This third step yields stars that are spatially and kinematically close to the photometrically young stars, but which cannot be identified as young based on their positions in the color-absolute magnitude diagram.

The outcome of the analysis up to the point of the third step is shown in Figure 1. To enable a selection cut that filters out field-star contaminants, we also compute a weight metric, defined such that the group member with the smallest core distance has a weight of 1, the group member with the greatest core distance has a weight of 0, and weights for the other group members are log-normally distributed between these two extremes. In Figure 1, we show 12,436 objects with weight exceeding 0.02 as gray points, and overplot 4,763 objects with weights exceeding 0.10 as black points.² The previously known δ Lyr cluster is visible at $(l, b) = (68^\circ, 15^\circ)$ and $(v_l, v_b) = (-4.5 \text{ km s}^{-1}, -4 \text{ km s}^{-1})$. RSG-5 is visible at $(l, b) = (83^\circ, 6^\circ)$, $(v_l, v_b) = (5.5 \text{ km s}^{-1}, -3.5 \text{ km s}^{-1})$. Most of the other subclusters, including in Cep-Cyg $(l, b = 90^\circ, 7^\circ)$ and Cerberus $(l, b = 48^\circ, 18^\circ)$ are too small or dispersed to have previously been analyzed in great detail.

Our fourth and final step was to cross-match the candidate Cep-Her member list against all known Kepler Objects of Interest. We used the Cumulative KOI table from the NASA Exoplanet Archive from 27 March 2022, and also compared against the `q1_q17_dr25` table (Thompson et al. 2018).

From the candidate members with weights exceeding 0.02, this yielded 11 known false positives, 6 “confirmed” planets, and 8 “candidate” planets. Inspection of the Kepler data validation summaries and Robovetter classifications for these objects showed whether they were potentially consistent with being *i*) planets, and *ii*) $\lesssim 10^8$ years old, based on the presence of rotational modulation at the expected period and amplitude (e.g., Rebull et al. 2020, Figure 9). Four objects remained after this inspection: Kepler-1627, Kepler-1643, KOI-7368, and KOI-7913.³

Figure 1 shows the positions of the KOIs along various projections. Kepler-1643 is near the core RSG-5 population both spatially and kinematically. KOI-7368 and KOI-7913 are in a diffuse region $\approx 40 \text{ pc}$ above RSG-5 in Z and $\approx 100 \text{ pc}$ closer to the Sun in Y . In tangential galactic velocity space, there is some kinematic overlap between the region the latter two KOIs are in and the main RSG-5 group.

We define two sets of stars in the local vicinity of our objects of interest. For candidate RSG-5 members, we require:

$$\begin{aligned} X/\text{pc} &\in [45, 75] \\ Y/\text{pc} &\in [320, 350] \\ Z/\text{pc} &\in [40, 70] \\ v_b/\text{km s}^{-1} &\in [-4, -3] \\ v_{l^*}/\text{km s}^{-1} &\in [4, 6] \end{aligned}$$

For the diffuse stars near KOI-7368 and KOI-7913, we require

$$\begin{aligned} X/\text{pc} &\in [20, 70] \\ Y/\text{pc} &\in [230, 270] \\ Z/\text{pc} &\in [75, 105] \\ v_b/\text{km s}^{-1} &\in [-3.5, -1.5] \\ v_{l^*}/\text{km s}^{-1} &\in [2, 6] \end{aligned}$$

and we call this latter set of stars “CH-2”. These cuts yield 141 candidate RSG-5 members, and 37 candidate CH-2 members. Tables of these stars are enumerated in Appendix A. An important consideration, especially for CH-2, is the contamination rate by field stars. We assess this in the following section.

2.3. The Cluster’s Age

2.3.1. Color-Absolute Magnitude Diagram

Color-absolute magnitude diagrams (CAMDs) of the candidate RSG-5 and CH-2 members are shown in the upper

² These counts only include objects with reliable astrometry and photometry: $\sigma/\sigma_{\text{fit}} > 5$; $G/\sigma_G > 50$; $G_{\text{RP}}/\sigma_{G_{\text{RP}}} > 20$; $G_{\text{BP}}/\sigma_{G_{\text{BP}}} > 20$.

³ These figures in fact give an estimate of the size of Cep-Her: if our 4/14 possible matches represent the true positive rate, then multiplying by the number of stars above our weight threshold (12,436) yields $\approx 3,500$ stars in the complex.

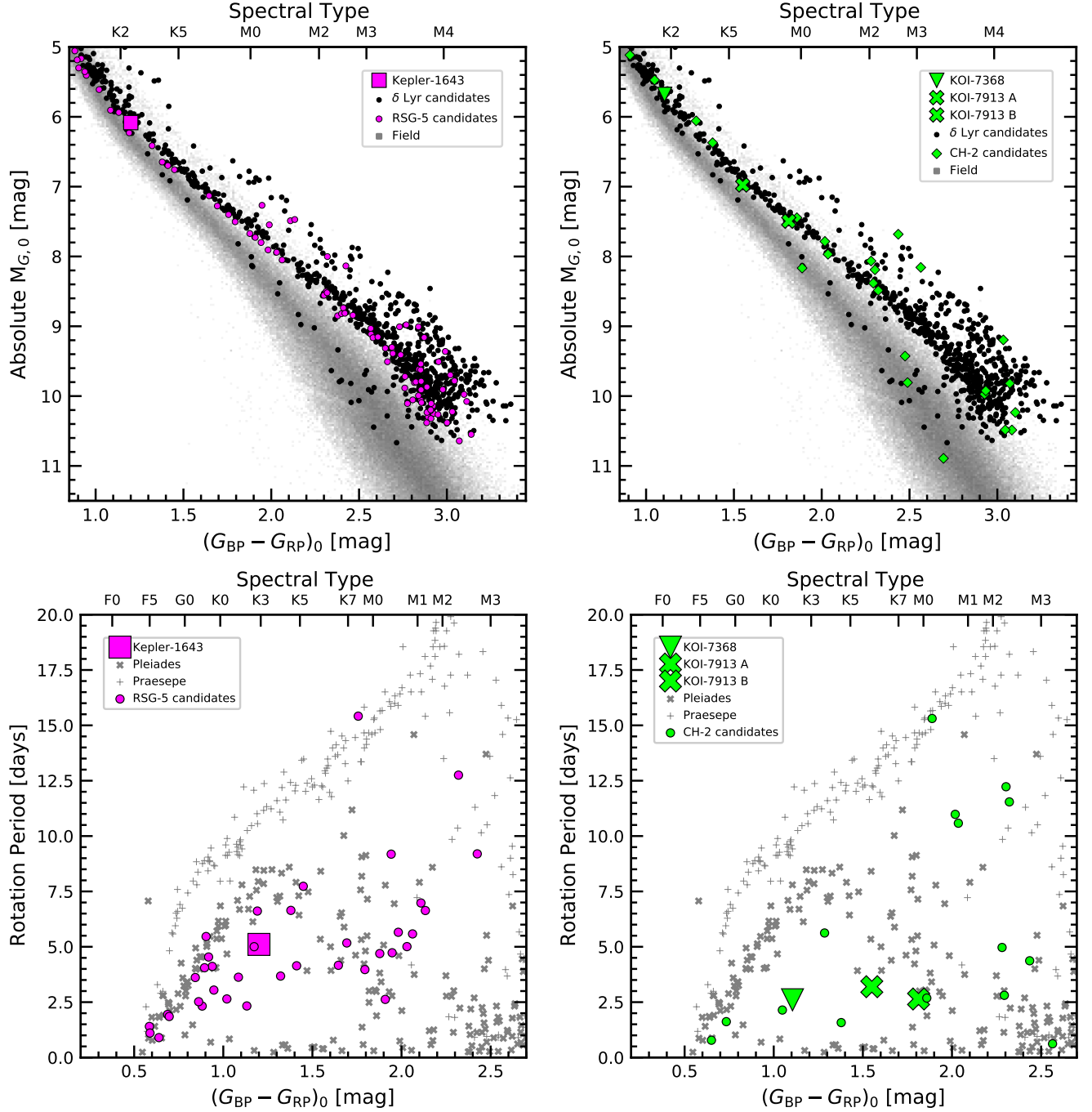


Figure 2. The stellar groups near KOI-7368, KOI-7913, and Kepler-1643 are 40 to 50 million years old. *Top row:* Color-absolute magnitude diagram of candidate Cep-her members, plotted over candidate members of the δ Lyr cluster (≈ 38 Myr; Bouma et al. 2022) and the Gaia EDR3 Catalog of Nearby Stars (gray background). The left and right columns shows stars in RSG-5 and CH-2, respectively. The range of colors is truncated to emphasize the pre-main-sequence. Stars that fall far below the cluster sequences are field interlopers. *Bottom row:* TESS and ZTF-derived stellar rotation periods, with the Pleiades (≈ 112 Myr) and Praesepe (≈ 650 Myr) shown for reference (Rebull et al. 2016; Douglas et al. 2017). The detection efficiency for reliable rotation periods falls off beyond $(G_{BP} - G_{RP})_0 \gtrsim 2.6$.

row of Figure 2. The stars from the δ Lyr cluster are from Bouma et al. (2022), and the field stars are from the Gaia EDR3 Catalog of Nearby Stars (Gaia Collaboration et al. 2021b). To make these diagrams, we imposed the data filtering criteria from Gaia Collaboration et al. (2018a, Appendix B), which include binaries while omitting instrumental artifacts from for instance low photometric signal to noise, or a small number of visibility periods. We then corrected for extinction using the Lallement et al. (2018)⁴ dust maps and the extinction coefficients $k_X \equiv A_X/A_0$ from Gaia Collaboration et al. (2018a), assuming that $A_0 = 3.1E(B-V)$. This yielded a mean and standard deviation for the reddening of $E(B-V) = 0.036 \pm 0.002$ for RSG-5, and $E(B-V) = 0.017 \pm 0.001$ for CH-2. By way of comparison, in Bouma et al. (2022) the same query for the δ Lyr cluster yielded $E(B-V) = 0.032 \pm 0.006$. Finally, for the plots we set the $(G_{BP} - G_{RP})_0$ color range to best visualize the region of maximal age information content: the pre-main-sequence.

The CAMDs show that for RSG-5, almost all of our candidate members are on a tight pre-main-sequence locus. This implies a false positive rate of a few percent, at most. By comparison, our control sample (the δ Lyr candidates) has a false positive rate of $\approx 12\%$, based on the number of stars that photometrically overlap with the field population, rather than the bulk cluster population. For CH-2, our membership selection gives 27 objects in the color range displayed, and 23 of them appear to be consistent with being on the pre-main-sequence. This implies a false positive rate in CH-2 of $\approx 15\%$.

Figure 2 also shows that most RSG-5 and CH-2 members overlap with the δ Lyr cluster, and that the groups are therefore roughly the same age. To quantify this, we use the empirical method introduced by Gagné et al. (2020, their Section 6.3). This idea is to fit the pre-main-sequence loci of a set of reference clusters, and to then model the locus of the target cluster as a linear combination of these reference cluster loci. For our reference clusters, we used UCL, IC 2602, and the Pleiades, with the memberships reported by Damiani et al. (2019) and Cantat-Gaudin et al. (2018) respectively. We adopted ages of 16 Myr for UCL (Pecaut & Mamajek 2016), 38 Myr for IC 2602⁵, and 112 Myr for the Pleiades (Dahm 2015). These assumptions and the subsequent processing steps taken to exclude field stars and binaries were identical to those described in Bouma et al. (2022). The mean and uncertainty of the resulting age posterior are 46^{+9}_{-7} Myr for RSG-5, and 36^{+10}_{-8} Myr for CH-2. For comparison, the

this procedure yields an age for the δ Lyr cluster of 38^{+6}_{-5} Myr. The slightly older isochronal age of RSG-5 is consistent with its location relative to the δ Lyr cluster in the upper left panel of Figure 2.

2.3.2. Stellar Rotation Periods

An independent way to assess the age of the candidate cluster members is to measure their stellar rotation periods. This approach can be achieved using surveys such as TESS (Ricker et al. 2015) and the Zwicky Transient Facility (ZTF, Bellm et al. 2019); it leverages a storied tradition of measuring rotation periods of stars in benchmark open clusters (see e.g., Skumanich 1972; Curtis et al. 2020). The TESS data in our case are especially useful, since they provide 3 to 5 lunar months of photometry for all of our candidate CH-2 and RSG-5 members.

We selected stars suitable for gyrochronology by requiring $(G_{BP} - G_{RP})_0 \geq 0.5$ to focus on FGKM stars that experience magnetic braking. For TESS, we also restricted our sample to $G < 16$, to ensure the stars are bright enough to extract usable light curves from the full-frame images (FFIs). The magnitude cut corresponds to $(G_{BP} - G_{RP})_0 < 2.6$ ($\sim M3V$) at the relevant distances. These cuts gave 19 stars in CH-2 and 42 stars in RSG-5. We extracted light curves from the TESS images using the `unpopular` package (Hattori et al. 2021), and regressed them against systematics with its causal pixel model. We measured rotation periods using Lomb-Scargle periodograms and visually vetted the results using an interactive program that allows us to switch between TESS Cycles, select particular sectors, flag stars with multiple periods, and correct half-period harmonics. For ZTF, we used the same color cut to focus on FGKM stars, but restricted the sample to $13 < G < 18$ to avoid the saturation limit on the bright end and ensure sufficient photometric precision at the faint end. We followed the procedure outlined in Curtis et al. (2020): we downloaded $8' \times 8'$ image cutouts, ran aperture photometry for the target and neighboring stars identified with Gaia, and used them to define a systematics correction to refine the target light curves.

The lower panels of Figure 2 show the results. In RSG-5, 36/42 stars have rotation periods faster than the Pleiades (86%). This numerator omits the two stars with periods > 12 days visible in the lower-left panel of Figure 2. The age interpretation for these latter stars, particularly the $\approx M2.5$ dwarf, is not obvious. Rebull et al. (2018) for instance have found numerous M-dwarfs with 10-12 day rotation periods at ages of USco (~ 8 Myr), and some may still exist at ages of LCC (~ 16 Myr; L. Rebull in preparation). Regardless, given that nearly no field star outliers seem to be present on the RSG-5 CAMD, the fact that we do not detect rotation periods for $\approx 14\%$ of stars should perhaps be taken as an indication for the fraction of stars for which rotation periods might not

⁴ <https://stilism.obspm.fr/>

⁵ Ages for IC 2602 vary from 40 to 46 Myr based on lithium-depletion-boundary (LDB) measurements (Dobbie et al. 2010; Randich et al. 2018), and from 30 to 46 Myr based on isochronal analyses (Stauffer et al. 1997; David & Hillenbrand 2015; Bossini et al. 2019).

be detectable, due to *e.g.*, pole-on stars having lower amplitude starspot modulation.

For CH-2, 13/19 stars have rotation periods that are obviously faster than their counterparts in the Pleiades (68%). 4 stars, not included in the preceding numerator, are M-dwarfs with rotation periods between 10 and 12.5 days. As just discussed, the age interpretation for these M-dwarfs is not obvious. Regardless, the $\approx 15\%$ false positive rate determined from the CAMD seems consistent with our fraction of detected rotation periods, given that RSG-5 was also missing rotation period detections for $\approx 15\%$ of its candidate members, which all seemed photometrically consistent with being part of a single pre-main-sequence locus.

It is challenging to convert these stellar rotation periods to a precise age estimate, since on the pre-main-sequence the stars are spinning up due to thermal contraction rather than down due to magnetized braking. Regardless, the rotation period distributions of both CH-2 and RSG-5 seem consistent with other 30 Myr to 50 Myr clusters (*e.g.*, IC 2602 and IC 2391; Douglas et al. 2021). They also seem consistent with the estimated false positive rates determined from the color-absolute magnitude diagrams.

3. THE STARS

Some salient stellar properties of the Kepler objects in Cep-Her can be gleaned from Figure 2. They span spectral types of G8V (Kepler-1627) to K6V (KOI-7913 A). The secondary in the KOI-7913 system has spectral type $\approx K8V$. And since a Solar-mass star with solar metallicity arrives at the zero-age main sequence at $t \approx 40$ Myr (Choi et al. 2016), these stars are all in the late stages of their pre-main-sequence contraction. Their heliocentric distances are ≈ 260 pc (KOI-7913 and KOI-7368, in CH-2) and ≈ 340 pc (Kepler-1643, in RSG-5).

The adopted stellar parameters are listed in Table 1. The stellar surface gravity, radius, mass, and density are found by interpolating against the MIST isochrones (Choi et al. 2016). The statistical uncertainties from this technique mostly originate from the parallax uncertainties; the systematic uncertainties are taken to be the absolute difference between the PARSEC (Bressan et al. 2012) and MIST isochrones. Reported uncertainties are a quadrature sum of the statistical and systematic components.

To verify these parameters and to also analyze spectroscopic youth proxies such as the Li I 6708 Å doublet and H α , we acquired spectra. We also acquired high resolution imaging for each system, to constrain the existence of visual companions, including possible bound binaries. The system-by-system details follow, and the relevant results are also summarized in Table 1.

3.1. Kepler 1643

Table 1. Selected system parameters of Kepler-1643, KOI-7368, and KOI-7913.

Parameter	Value	Uncertainty	Comment
<i>Kepler-1643</i>			
<i>Stellar parameters:</i>			
Gaia G [mag]	13.836	± 0.003	A
T_{eff} [K]	4916	± 110	B
$\log g_*$ [cgs]	4.502	± 0.035	C
R_* [R_\odot]	0.855	± 0.044	C
M_* [M_\odot]	0.845	± 0.025	C
ρ_* [g cm^{-3}]	1.910	± 0.271	C
P_{rot} [days]	5.106	± 0.044	D
Li EW [mÅ]	130	+6, -5	E
<i>Transit parameters:</i>			
P [days]	5.3426258	± 0.0000101	D
R_p/R_*	0.025	± 0.001	D
b	0.58	± 0.05	D
R_p [R_\oplus]	2.32	± 0.14	D
t_{14} [hours]	2.409	± 0.061	D
<i>KOI-7368</i>			
<i>Stellar parameters:</i>			
Gaia G [mag]	12.831	± 0.004	A
T_{eff} [K]	5241	± 50	F
$\log g_*$ [cgs]	4.499	± 0.030	C
R_* [R_\odot]	0.876	± 0.035	C
M_* [M_\odot]	0.879	± 0.018	C
ρ_* [g cm^{-3}]	1.840	± 0.225	C
P_{rot} [days]	2.606	± 0.038	D
Li EW [mÅ]	236	+16, -14	E
<i>Transit parameters:</i>			
P [days]	6.8430341	± 0.0000125	D
R_p/R_*	0.023	± 0.01	D
b	0.50	± 0.06	D
R_p [R_\oplus]	2.22	± 0.12	D
t_{14} [hours]	2.792	± 0.075	D
<i>KOI-7913</i>			
<i>Stellar parameters:</i>			
Gaia G [mag]	14.200	± 0.003	A
$T_{\text{eff,A}}$ [K]	4324	± 70	B
$T_{\text{eff,B}}$ [K]	4038	± 70	B
$\log g_{*,A}$ [cgs]	4.523	± 0.043	C
$R_{*,A}$ [R_\odot]	0.790	± 0.049	C
$M_{*,A}$ [M_\odot]	0.760	± 0.025	C
$\rho_{*,A}$ [g cm^{-3}]	2.172	± 0.379	C
$P_{\text{rot,A}}$ [days]	3.387	± 0.016	D
$P_{\text{rot,B}}$ [days]	2.642	± 0.067	D
(Li EW) _A [mÅ]	65	+8, -6	E
(Li EW) _B [mÅ]	42	+12, -19	E
ΔG_{AB} [mag]	0.51	± 0.01	F
Apparent sep. [au]	959.4	± 1.9	F
<i>Transit parameters:</i>			
P [days]	24.2785706	± 0.0002630	D
R_p/R_*	0.027	± 0.001	D
b	0.30	± 0.15	D
R_p [R_\oplus]	2.34	± 0.18	D
t_{14} [hours]	4.396	0.207	D

NOTE— (A) Gaia Collaboration et al. (2021a). (B) HIRES SpecMatch-Emp (Yee et al. 2017). (C) Cluster isochrone (Choi et al. 2016; Bressan et al. 2012). (D) Kepler light curve. The full set of transit parameters are given in Appendix C. (E) HIRES (Bouma et al. 2021). (F) TRES SPC (Buchhave et al. 2010; Bieryla et al. 2021). (G) Magnitude difference and physical distance between primary and secondary; from Gaia EDR3. (H) HIRES SpecMatch-Synth (Petigura et al. 2017).

Spectra—For Kepler-1643, we acquired two iodine-free spectra from Keck/HIRES on the nights of 2020 Aug 16 and 2021 Oct 25. The acquisition and analysis followed the usual techniques of the California Planet Survey (Howard et al. 2010). We derived the stellar parameters (T_{eff} , $\log g$, R_*) using SpecMatch-Emp (Yee et al. 2017), which yielded values in $< 1\text{-}\sigma$ agreement with those from the cluster-isochrone method. This approach also yielded $[\text{Fe}/\text{H}] = 0.13 \pm 0.09$. Using the broadened synthetic templates from SpecMatch-Synth (Petigura et al. 2017), we found $v \sin i = 9.3 \pm 1.0 \text{ km s}^{-1}$. The systemic radial velocity at the two sequence epochs was $-9.1 \pm 1.9 \text{ km s}^{-1}$ and $-7.8 \pm 1.2 \text{ km s}^{-1}$ respectively. To infer the equivalent width of the Li I 6708 Å doublet, we followed the procedure described by Bouma et al. (2021). This yielded a strong detection: $\text{EW}_{\text{Li}} = 130^{+6}_{-5} \text{ mÅ}$, with values consistent at $< 1\text{-}\sigma$ between the two epochs. The quoted value does not correct for the Fe I blend at 6707.44 Å, because HIRES resolves the two features.

High-Resolution Imaging—We acquired adaptive optics imaging of Kepler-1643 on the night of 2019 June 28 using the NIRC2 imager on Keck-II. Using the narrow camera (FOV = $10.2''$), we obtained 4 images in the K' filter ($\lambda = 2.12 \mu\text{m}$) with a total exposure time of 320 s. We analyzed these data following Kraus et al. (2016), and determined the detection limits to visual companions by analyzing the residuals after subtracting an empirical PSF template. This procedure yielded contrast limits of $\Delta K' = 4.1 \text{ mag}$ at $\rho = 150 \text{ mas}$, $\Delta K' = 5.8 \text{ mag}$ at $\rho = 300 \text{ mas}$, and $\Delta K' = 8.3 \text{ mag}$ at $\rho > 1000 \text{ mas}$.

3.2. KOI-7368

Spectra—For KOI-7368, we acquired a spectrum on 2015 June 1 using the echelle spectrograph (TRES; Fűrész et al. 2008) mounted at the Tillinghast 1.5m at the Fred Lawrence Whipple Observatory. The stellar parameter classification pipeline for the TRES spectra has been described by Bieryla et al. (2021). It is based on the synthetic template library originally constructed by Buchhave et al. (2010). The resulting stellar parameters (T_{eff} , $\log g$, R_*) agreed with those from the cluster-isochrone method within $1\text{-}\sigma$, though the effective temperature was more precise by a factor of three. Auxiliary spectroscopic parameters included the metallicity $[\text{Fe}/\text{H}] = -0.02 \pm 0.08$, the equatorial velocity $v \sin i = 20.21 \pm 0.50 \text{ km s}^{-1}$, and the systemic velocity $\text{RV}_{\text{sys}} = -10.9 \pm 0.2 \text{ km s}^{-1}$. The Li 6708 Å EW measurement procedure yielded $\text{EW}_{\text{Li}} = 236^{+16}_{-14} \text{ mÅ}$.

High-Resolution Imaging—We acquired adaptive optics imaging of KOI-7368 on the night of 2019 June 12, again using NIRC2. The observational configuration and reduction was identical as for Kepler-1643. No companions were detected,

and the analysis of the image residuals yielded contrast limits of $\Delta K' = 5.2 \text{ mag}$ at $\rho = 150 \text{ mas}$, $\Delta K' = 6.7 \text{ mag}$ at $\rho = 300 \text{ mas}$, and $\Delta K' = 8.7 \text{ mag}$ at $\rho > 1000 \text{ mas}$.

3.3. KOI-7913

Binarity—KOI-7913 is almost certainly a binary. The north-west primary is ≈ 0.5 magnitudes brighter than the south-east secondary in optical passbands. The two stars are separated in Gaia EDR3 by $3''.5$ on-sky, and have parallaxes consistent within $1\text{-}\sigma$ (with an average $\varpi = 3.66 \pm 0.01 \text{ mas}$). The apparent on-sky separation is $959 \pm 2 \text{ au}$. The Gaia EDR3 proper motions are also nearly identical. Since two stars were resolved in the Kepler Input Catalog and are roughly one Kepler pixel apart, an accurate crowding metric has already been applied in the NASA Ames data products to correct the mean flux level (Morris et al. 2017). This is important for deriving accurate transit depths.

Spectra—We acquired Keck/HIRES spectra for KOI-7913 A on the night of 2021 Nov 13, and KOI-7913 B on the night of 2021 Oct 26. The SpecMatch-Emp (Yee et al. 2017) machinery yielded $T_{\text{eff,A}} = 4324 \pm 70 \text{ K}$, $T_{\text{eff,B}} = 4038 \pm 70 \text{ K}$. The remaining parameters were in agreement with those from the cluster isochrone. For the primary, we also found $[\text{Fe}/\text{H}] = -0.06 \pm 0.09$, $v \sin i = 13.3 \pm 1.0 \text{ km s}^{-1}$, and $\text{RV}_{\text{sys}} = -17.8 \pm 1.1 \text{ km s}^{-1}$. For the secondary, these same parameters were $[\text{Fe}/\text{H}] = -0.01 \pm 0.09$, $v \sin i = 10.7 \pm 1.0 \text{ km s}^{-1}$, and $\text{RV}_{\text{sys}} = -18.8 \pm 1.1 \text{ km s}^{-1}$. Neither of the KOI-7913 components shows strong lithium absorption, but this is expected given their $\approx \text{K6V}$ and $\approx \text{K8V}$ spectral types. They do however both show $\text{H}\alpha$ in emission. We discuss the significant in greater depth in Appendix B, but broadly speaking both observations are consistent with a $\approx 40 \text{ Myr}$ age for KOI-7913.

High-Resolution Imaging—We acquired adaptive optics imaging of KOI-7913 on the night of 2020 Aug 27 using the NIRC2 imager. The observational configuration and reduction was identical as before. The images showed KOI-7913 A, KOI-7913 B, and an additional faint star $\approx 0''.99$ due East of KOI-7913 B. Applying the PSF-fitting routines from Kraus et al. (2016), the tertiary star has a separation $\rho = 4397 \pm 3 \text{ mas}$ from the primary, at a position angle $231.17^\circ \pm 0.02^\circ$, with a $\Delta K' = 6.97 \pm 0.04$. While it is too faint to affect the interpretation of the KOI itself, it would be amusing if the faint neighbor were also comoving and young – at the age of the system, it would have a mass roughly between 10 and 15 M_{Jup} . Additional imaging epochs will tell.

4. THE PLANETS

4.1. Kepler Data

The Kepler space telescope observed Kepler-1643, KOI-7913, and KOI-7368 at a 30-minute cadence between May 2009 and April 2013. For all three systems quarters 1 through



Figure 3. Raw and processed light curves for the Kepler Objects of Interest in Cep-Her. *Top:* 50 day light curve segment from the 3.9 years of Kepler data. The ordinate shows the PDCSAP median-subtracted flux in units of parts-per-thousand ($\times 10^{-3}$). The dominant signal is induced by starspots. *Bottom:* Phase-folded transits of Kepler-1643, KOI-7913, KOI-7368, and Kepler-1627 with stellar variability removed. The maximum *a posteriori* transit model is shown with the gray line, and the residual after subtracting the transit model is vertically displaced. Windows over 10 hours are shown. Gray points are individual flux measurements; black points are binned to 20 minute intervals, and have a representative 1- σ error bar in the center-right of each panel.

17 were observed with minimal data gaps. The top panel of Figure 3 shows a 50-day slice of the PDCSAP light curves for the three new Cep-Her candidates, along with Kepler-1627. In PDCSAP, nonastrophysical variability is removed through a cotrending approach that uses a set of basis vectors derived by applying singular value decomposition to a set of systematics-dominated light curves (Smith et al. 2017). In our analysis, we used the PDCSAP light curves with the default optimal aperture (Smith et al. 2016). Cadences with non-zero quality flags were omitted. In all cases, the stars are dominated by spot-induced modulation with peak-to-peak variability between 2% and 10%. These signals are much larger than the transits, which have depth $\approx 0.1\%$. To quantify the stellar rotation periods, we calculated the Lomb-Scargle periodogram for each Kepler quarter independently. The resulting means and standard deviations are in Table 1.

4.2. Transit and Stellar Variability Model

Our goals in fitting the Kepler light curves are twofold. First, we want to derive accurate planetary sizes and orbital properties. Second, we want to remove the stellar variability signal to enable a statistical assessment of the probability that the transit signals are planetary.

Our adopted approach was as follows. Given an initial guess for the transit ephemeris from the `q1_q17_dr25` analysis (Thompson et al. 2018), the light curve was first trimmed to a local window around each transit, spanning $\pm 3 \times t_{14}$. The local out-of-transit points were then fitted with a fourth-order polynomial, which was then divided out from the light curve. The resulting flattened transits were then fitted with a planetary transit under the assumption of quadratic limb darkening. Our model therefore included 8 free parameters for the transit ($\{P, t_0, \log R_p/R_*, b, u_1, u_2, R_*, \log g\}$), 2 free parameters for the light curve normalization and a white noise jitter ($\{f, \sigma_f\}$), and an additional 5 implicit parameters per transit through the polynomial.

We fitted the models using `exoplanet` (Foreman-Mackey et al. 2020). We assumed a Gaussian likelihood, and sampled using `PyMC3`’s No-U-Turn Sampler (Hoffman & Gelman 2014), after having initialized using the maximum *a posteriori* (MAP) model. We used the Gelman & Rubin (1992) statistic (\hat{R}) as our convergence diagnostic. The resulting fits are shown in the lower panels of Figure 3, and the important derived parameters are in Table 1. The set of full parameters with their priors are given in Appendix C.

One weakness of our fitting approach is that we have fixed 5 implicit parameters per individual transit to their MAP values to remove the stellar variability signal. An alternative could be to fit the planetary transits simultaneously with the starspot-induced variability using, say, a quasiperiodic Gaussian process (GP). We explored this approach, but found that it required careful fine-tuning of the hyperparameter priors,

otherwise the GP would tend to incorporate variability that was not part of the transit, even if it was short-term variability attributable to flares, or simply instrumental noise. This failure mode is somewhat pernicious, in that it yields an ill-founded sense of confidence in an “overly clean” transit model fit. While our model is simpler, it has the benefit that the white noise jitter never trades off with any parameter equivalent to a damping timescale for the coherence of the GP. It is also computationally efficient, and it captures the planetary parameters that we actually care about.

4.3. Planet Validation

In the future, it may be possible to obtain independent evidence for the Cep-Her planets to directly confirm their planetary nature. The most likely path would be through transit observations using a high-resolution spectrograph (see Bouma et al. 2022). In the interim, it is of interest whether the transit signals could be astrophysical false positives, or whether they can be argued to be planetary on a statistical basis. We adopt the Bayesian framework implemented in `VESPA` for this purpose (Morton 2012, 2015). Briefly summarized, the priors in `VESPA` take as given the binary star occurrence rate from Raghavan et al. (2010), direction-specific star counts from Girardi et al. (2005), and planet occurrence rates as described by Morton (2012, Section 3.4). The likelihoods are then evaluated by forward-modeling a synthetic population of eclipsing bodies for each possible astrophysical model class, in which each population member has a particular trapezoidal eclipse depth, total duration, and ingress duration. These summary statistics are then compared against the actual photometric data to evaluate the probabilities of false positive scenarios such as foreground eclipsing binaries, hierarchical eclipsing binaries, and background eclipsing binaries.

Kepler-1643—Kepler-1643 b (KOI-6186.01) was already validated as a transiting planet by Morton et al. (2016), who found a probability for any of the aforementioned false positive scenarios of 9×10^{-6} . Repeating the calculation with our own stellar-variability correction and the new NIRC2 imaging constraints, we find $\text{FPP} = 6 \times 10^{-9}$, where the improvement is due to the new NIRC2 contrast curves. Figure 3 shows the justification: the transit is flat and has a high S/N (≈ 47), which is difficult to reproduce with eclipsing binary models.

Intriguingly, Kepler-1643 formally failed one of the centroid shift tests (see the `q1_q17_dr25_koi` data release): the angular distance between the target star’s catalog position and the position of the transiting source was measured as $1''.0$ at $4.4\text{-}\sigma$. The reports show however that two outlying quarters (2 and 6) drive the offset – the centroid locations from the other Kepler quarters are consistent at $\lesssim 0''.4$. Nonetheless, this is an instructive exercise in how stellar variability complicates centroid-based vetting tests. The centroid shifts

measured by these tests are determined from the in- and out-of-transit flux-weighted centroids. For stars with significant spot-induced variability there is no static baseline in either the in- or out-of-transit phases.

KOI-7368—KOI-7368.01 is listed on the NASA Exoplanet Archive as a “candidate” planet. Morton et al. (2016) did not compute a false positive probability for the system because their default trapezoidal fitting routine failed, presumably due to the spot-induced variability. Our fitting approach rectifies this point, and our new NIRC2 images revealed no new stellar companions. Performing the validation calculation, we find $FPP \approx 4 \times 10^{-3}$. Though not as convincing as Kepler-1643, this formally clears the usual threshold for calling the planet statistically validated (Morton 2012). The S/N of the transit is ≈ 32 , which indicates that it is unlikely to be caused by systematic noise in the light curve (see Figure 3). The positional probability score also meets the requirements for transiting sources thought to share positions with their target stars (Morton et al. 2016; Bryson & Morton 2017).

It bears mentioning that KOI-7368 shows a weak centroid shift in the q1_q17_dr25_koi validation reports, similar to Kepler-1643. For KOI-7368, the reported offset is smaller, and less statistically significant ($0''.2$; $3.0\text{-}\sigma$). Again, the data validation reports show that the shift is caused by a few outlying quarters (4, 5, 8, and 12). The fact that the remaining data show a consistent scatter between centroid locations suggests that these outliers are also caused by the stellar variability. Independently, our imaging shows that there are no neighboring sources that could cause an offset of the observed amplitude.

KOI-7913—KOI-7913.01 is also listed on the NASA Exoplanet Archive as a “candidate” planet. The canonical Morton et al. (2016) analysis was of Q1-Q17 KOIs from DR24, and therefore spanned KOI-1.01 to KOI-7620.01 and omitted KOI-7913.01. However the results of the subsequent DR25 analysis by Morton et al. are listed at the NASA Exoplanet Archive. The relevant table gives a probability for the system being an astrophysical false positive of 1.4×10^{-4} , with the most likely false positive scenario being a blended eclipsing binary. Repeating the calculation with our new detrending and contrast curves, we find a similar result: $FPP = 1.3 \times 10^{-4}$. Though the transit has the lowest S/N of any of the objects discussed ($S/N = 14$), its lower FPP relative to KOI-7368 can be understood through its relatively flat-bottomed shape, combined with its long transit duration relative to plausible eclipsing binary models (Figure 3). The host star probability usability score (Bryson & Morton 2017) also meets the usual threshold, and so the planet seems to be validated. Its disposition has however previously fluctuated from “false positive” to “candidate”. The most likely explanation is the presence of KOI-7913 B, which is located

approximately one Kepler pixel away from Kepler-7913 A (see Appendix D). Our pixel-level analysis of the target pixel files did not show any evidence to support the idea that KOI-7913 B could host the transiting planet. Our NIRC2 imaging similarly ruled out the possibility of any other plausible host star for the planet other than KOI-7913 A.

5. DISCUSSION & CONCLUSION

5.1. Normal-Sized Mini-Neptunes Exist at 40 Myr

Current thinking about the origins and evolution of lose-in mini-Neptunes has recently been reviewed by Bean et al. (2021). In the context of the existing exoplanet population, the most significant novelty about Kepler-1643 b, KOI-7368.01, and KOI-7913 is that they have normal sizes. More specifically, the size distribution of mini-Neptunes spans $\approx 1.8 R_{\oplus}$ to $\approx 3.6 R_{\oplus}$, with a peak at $\approx 2.4 R_{\oplus}$ (Fulton et al. 2017, Figure 7). Figure 4 shows the sizes, orbital periods, and ages of known transiting planets, emphasizing those with precise ages. Considering planets younger than 10^8 years, the smallest previously known were AU Mic c ($\approx 3.0 \pm 0.2 R_{\oplus}$, averaging the results of Martioli et al. 2021 and Gilbert et al. 2022), Kepler-1627 Ab ($3.8 \pm 0.2 R_{\oplus}$; Bouma et al. 2022), and AU Mic d ($4.2 \pm 0.2 R_{\oplus}$; Plavchan et al. 2020). The other transiting planets younger than 10^8 years are much larger, with sizes between 4 and $10 R_{\oplus}$ (Mann et al. 2016; David et al. 2016; Benatti et al. 2019; David et al. 2019; Newton et al. 2019; Rizzuto et al. 2020; Bouma et al. 2020).

Run some evolutionary models, make some comments about the core mass, KH timescale, etc.

5.2. Is CH-2 really a star cluster?

RSG-5, and Kepler-1643’s membership inside it, clearly meet the typical expectations of a star claimed to be in an open cluster. RSG-5 shows an obvious overdensity relative to the local field population (e.g., Figure 1), and our membership selection easily produces a clean pre-main-sequence locus in color-absolute magnitude space (Figure 2). CH-2, and KOI-7913 and KOI-7368’s membership inside it, do not meet those expectations in as obvious a manner. This is because this association of stars is diffuse.

To quantify the density discrepancy, we can compare the spatial and velocity volumes searched to select candidate members of each cluster. For RSG-5, we drew 141 candidate members from a $30\text{pc} \times 30\text{pc} \times 30\text{pc}$ spatial cube, given a $1\text{km s}^{-1} \times 2\text{km s}^{-1}$ rectangle in apparent galactic velocity. For CH-2, our 37 candidate members came from a spatial cube of dimension $50\text{pc} \times 40\text{pc} \times 30\text{pc}$, and the velocity rectangle of $2\text{km s}^{-1} \times 4\text{km s}^{-1}$. If we define the “searched volume” in units of $\text{pc}^3(\text{km s}^{-1})^2$, then the volume ratio of CH-2:RSG-5 is $\approx 9:1$. The density (number of stars per unit searched volume) within RSG-5 relative to CH-2 similarly comes out to 34 to 1.

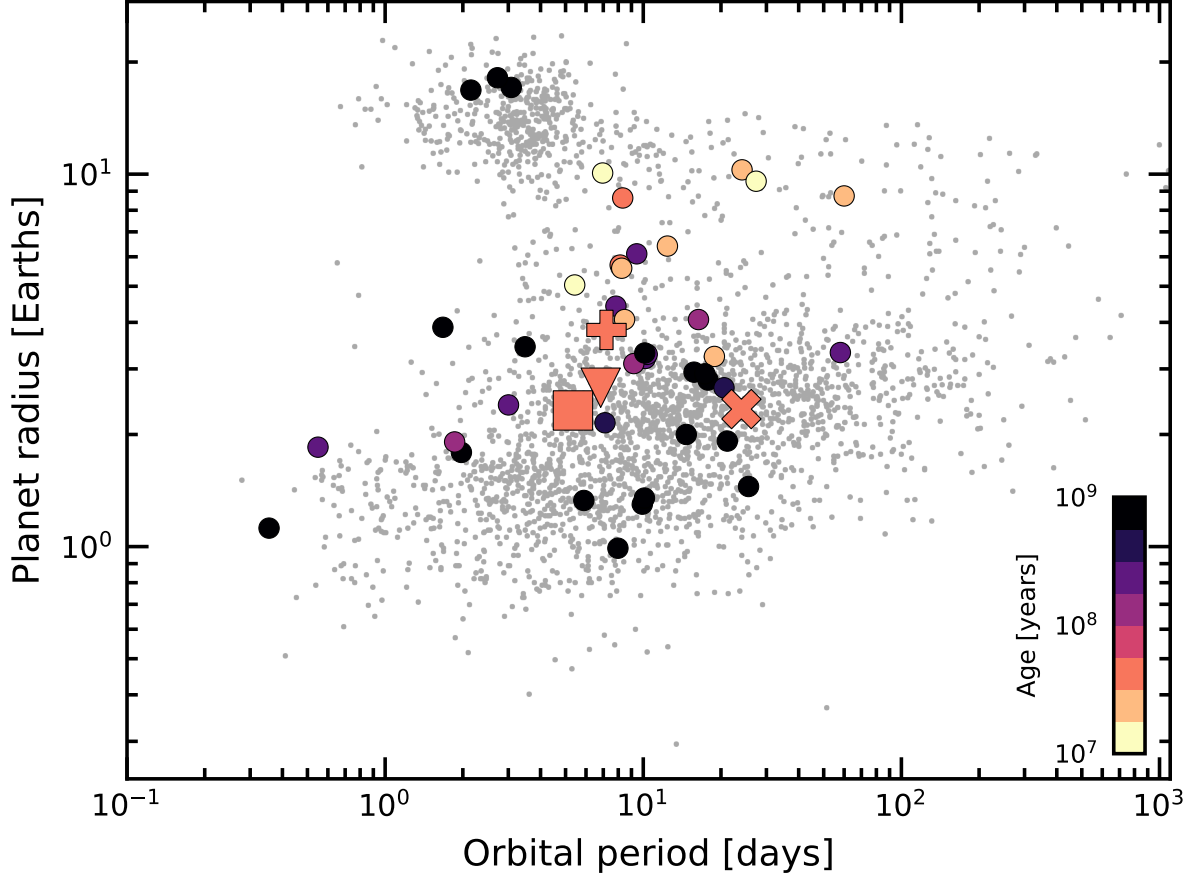


Figure 4. Radii, orbital periods, and ages of transiting exoplanets. Planets younger than a gigayear with $\tau/\sigma_\tau > 3$ are emphasized, where τ is the age and σ_τ is its uncertainty. Kepler-1627 (+), KOI-7368 (down-triangle), KOI-7913 (X), Kepler-1643 (diamond). The large sizes of the youngest transiting planets could be tied to a selection effect. Kepler-1643, KOI-7368, and KOI-7913 have normal mini-Neptune sizes of 2 to $3 R_\oplus$, which is a novelty given their ages. Parameters are from the NASA Exoplanet Archive (2022 Apr 5).

So what makes a star cluster? Historic answers to this question have recently been reviewed by [Krumholz et al. \(2019\)](#): some definitions that have been offered include criteria such as being gravitationally bound, and having a mass density that significantly exceeds the mean in a cluster’s galactic neighborhood. We prefer a modified version of the definition adopted by [Krumholz et al. \(2019\)](#): for our purposes a star cluster is a group of at least 12 stars that was physically associated at its time of formation. The somewhat arbitrary “12” is set to distinguish clusters from high-order multiple star systems. We therefore explicitly include dissolved clusters and their tidal tails in our concept of clusters. We also explicitly exclude the idea that a particular number of stars per unit spatial volume is required to define a cluster. The latter point acknowledges the fact that an important factor in cluster identification is now also the number per unit velocity volume, whether in 2-dimensional tangential velocity, or when including the third radial component. Perhaps once stellar rotation periods and chemical abundances reach the same level of ubiquity as stellar proper motions, they

might enable further refinement of our ability in cluster discovery.

From a data-driven perspective, how do we demonstrate that a star is in a cluster, *i.e.*, that it is part of a group of stars that was physically associated at its time of formation? Back-integrating the orbits is one convincing approach, but it does not always work ([CITE](#)). The relatively minimal approach suggested by [Tofflemire et al. \(2021\)](#) is intriguing: search for coeval, phase-space neighbors, measure their ages, and determine if they share a common age. This approach is more accurately described as a method for determining whether a star is currently associated with a set of coeval stars, which is much easier to determine than what the association looked like in the past. From this standard, our analysis thus far of CH-2 has already demonstrated the existence of such an association.

A crucial logical step in this method however is to ensure that the (automated) search process for coeval phase-space neighbors in fact produces neighbors at a rate different from what it would for field stars.

And so we ask: what is the density of field stars in the CH-2 region? If we had applied Ronan’s pre-main-sequence selection, + HDBScan, + local neighbors... what would we have gotten? Similarly... if you just applied Adam Kraus’ Comove What is the likelihood we are fooling ourselves?

5.3. Further Work on Cep-Her

Disentangling its kinematics * Need an RV survey.

Benchmarking its age(s): * Lithium analysis of FGK depletion (bright enough to be feasible).

* Asteroseismology of the delta Sct stars (TESS data are there, group is rich enough).

Finding more interesting objects in it: * Kepler data... presumably ~ 200 stars in the cluster were observed, in order to have detected 4 planets.

* TESS data

5.4. Summary

We have argued that Kepler-1643 b, KOI-7368 b, and KOI-7913 Ab *i*) are 40 to 50 million years old, and *ii*) that each signal is most likely planetary. The evidence for the planetary interpretation comes from an application of VESPA to the Kepler data, alongside new adaptive optics imaging from NIRC2. The validity of the VESPA framework rests on the premise that non-astrophysical false positives, including false alarms and known neighboring eclipsing binaries, can be rejected. Kepler-1643 and KOI-7368 both pass all but one of the canonical vetting checks: the check for centroid offsets between the in and out-of-transit phases. For both cases, we have argued the weak observed shifts seem to be caused by starspot-induced variability in specific quarters shifting the stellar center-of-light. In addition, our imaging rules out companions stars with the necessary brightness and position to explain the reported shifts.

Each system has multiple indicators of youth that support the reported ages. For Kepler-1643, perhaps the strongest youth indicator is its physical and kinematic association with RSG-5. Based on the color-absolute magnitude diagram, we are able to select members of this cluster with a false positive rate of $\ll 5\%$ (Figure 2); Kepler-1643 is one such member. While the stellar rotation period agrees with this assessment, its lithium content is somewhat low, which might motivate future exploration of lithium depletion across FGKM stars in RSG-5 (see Appendix B)

The spatio-kinematic argument for the youth of KOI-7368 and KOI-7913 is weaker because they are in an association of stars, CH-2, that is more diffuse. For KOI-7913, stronger indicators of its age come from its binary. Both stellar components in KOI-7913 have isochronal ages consistent with 40 Myr. Both components also show H α in emission, which for the $\approx K6V$ primary is a good indicator that the star is $\lesssim 100$ Myr old. For KOI-7368, which is slightly more mas-

sive, the Li 6708Å EW measurement and stellar rotation period are more constraining, and provide independent verification of the star’s youth.

ACKNOWLEDGMENTS

L.G.B. acknowledges support from the TESS GI Program (NASA grants 80NSSC19K0386 and 80NSSC19K1728) and the Heising-Simons Foundation (51 Pegasi b Fellowship). Keck/NIRC2 imaging was acquired by program 2015A/N301N2L (PI: A. Kraus). This paper also includes data collected by the TESS mission, which are publicly available from the Mikulski Archive for Space Telescopes (MAST). Funding for the TESS mission is provided by NASA’s Science Mission directorate. We thank the TESS Architects (G. Ricker, R. Vanderspek, D. Latham, S. Seager, J. Jenkins) and the many TESS team members for their efforts to make the mission a continued success. Finally, we also thank the Keck Observatory staff for their support of HIRES and remote observing. We recognize the importance that the summit of Maunakea has within the indigenous Hawaiian community, and are deeply grateful to have the opportunity to conduct observations from this mountain.

Software: *astrobase* (Bhatti et al. 2018), *astropy* (Astropy Collaboration et al. 2018), *astroquery* (Ginsburg et al. 2018), *exoplanet* (Foreman-Mackey et al. 2020), and its dependencies (Agol et al. 2020; Kipping 2013; Luger et al. 2019; Theano Development Team 2016), *PyMC3* (Salvatier et al. 2016), *scipy* (Jones et al. 2001), *VESPA* (Morton 2012, 2015),

Facilities: *Astrometry:* Gaia (Gaia Collaboration et al. 2018b, 2021a). *Imaging:* Second Generation Digitized Sky Survey. Keck:II (NIRC2; www2.keck.hawaii.edu/inst/nirc2). *Spectroscopy:* Tillinghast:1.5m (TRES; Fűrész et al. 2008). Keck:I (HIRES; Vogt et al. 1994). *Photometry:* Kepler (Borucki et al. 2010), TESS (Ricker et al. 2015).

REFERENCES

- Agol, E., Luger, R., & Foreman-Mackey, D. 2020, *AJ*, **159**, 123
- Arevalo, R. T., Tamayo, D., & Cranmer, M. 2022, [arXiv:2203.02805 \[astro-ph\]](https://arxiv.org/abs/2203.02805), arXiv: 2203.02805
- Astropy Collaboration, Price-Whelan, A. M., Sipőcz, B. M., et al. 2018, *AJ*, **156**, 123
- Bean, J. L., Raymond, S. N., & Owen, J. E. 2021, *Journal of Geophysical Research (Planets)*, **126**, e06639
- Bellm, E. C., Kulkarni, S. R., Graham, M. J., et al. 2019, *PASP*, **131**, 018002
- Benatti, S., Nardiello, D., Malavolta, L., et al. 2019, *A&A*, **630**, A81
- Berger, T. A., Howard, A. W., & Boesgaard, A. M. 2018, *ApJ*, **855**, 115
- Bhatti, W., Bouma, L. G., & Wallace, J. 2018, *astrobase*, <https://doi.org/10.5281/zenodo.1469822>
- Bieryla, A., Tronsgaard, R., Buchhave, L. A., et al. 2021, in *Posters from the TESS Science Conference II (TSC2)*, 124
- Borucki, W. J., Koch, D., Basri, G., et al. 2010, *Science*, **327**, 977
- Bossini, D., Vallenari, A., Bragaglia, A., et al. 2019, *A&A*, **623**, A108
- Bouma, L. G., Curtis, J. L., Hartman, J. D., Winn, J. N., & Bakos, G. A. 2021, [arXiv:2107.08050 \[astro-ph\]](https://arxiv.org/abs/2107.08050)
- Bouma, L. G., Hartman, J. D., Brahm, R., et al. 2020, *AJ*, **160**, 239
- Bouma, L. G., Curtis, J. L., Masuda, K., et al. 2022, *AJ*, **163**, 121
- Bouvier, J. 2020, *Mem. Soc. Astron. Italiana*, **91**, 39
- Bouvier, J., Barrado, D., Moraux, E., et al. 2018, *A&A*, **613**, A63
- Bressan, A., Marigo, P., Girardi, L., et al. 2012, *MNRAS*, **427**, 127
- Bryson, S. T., & Morton, Timothy, D. 2017, *Planet Reliability Metrics: Astrophysical Positional Probabilities for Data Release 25*, Kepler Science Document KSCI-19108-001, id. 16. Edited by Michael R. Haas and Natalie Batalha
- Buchhave, L. A., Bakos, G. A., Hartman, J. D., et al. 2010, *ApJ*, **720**, 1118
- Butler, R. P., Cohen, R. D., Duncan, D. K., & Marcy, G. W. 1987, *ApJL*, **319**, L19
- Campello, R. J. G. B., Moulavi, D., Zimek, A., & Sander, J. 2015, *ACM Transactions on Knowledge Discovery from Data*, **10**, 5:1
- Cantat-Gaudin, T., Jordi, C., Vallenari, A., et al. 2018, *A&A*, **618**, A93
- Choi, J., Dotter, A., Conroy, C., et al. 2016, *ApJ*, **823**, 102
- Collins, J. M., Jones, H. R. A., & Barnes, J. R. 2017, *a*, **602**, A48
- Curtis, J. L., Agüeros, M. A., Mamajek, E. E., Wright, J. T., & Cummings, J. D. 2019, *AJ*, **158**, 77
- Curtis, J. L., Agüeros, M. A., Matt, S. P., et al. 2020, *ApJ*, **904**, 140
- Dahm, S. E. 2015, *ApJ*, **813**, 108
- Damiani, F., Prisinzano, L., Pillitteri, I., Micela, G., & Sciortino, S. 2019, *A&A*, **623**, A112
- David, T., Hillenbrand, L., & Petigura, E. 2016, *Nature*, **534**, 658
- David, T. J., & Hillenbrand, L. A. 2015, *ApJ*, **804**, 146
- David, T. J., Petigura, E. A., Luger, R., et al. 2019, *ApJL*, **885**, L12
- Dawson, R. I., & Johnson, J. A. 2018, *ARA&A*, **56**, 175
- Dinnbier, F., & Kroupa, P. 2020, *a*, **640**, A85
- Dobbie, P. D., Lodieu, N., & Sharp, R. G. 2010, *MNRAS*, **409**, 1002
- Douglas, S. T., Agüeros, M. A., Covey, K. R., & Kraus, A. 2017, *ApJ*, **842**, 83
- Douglas, S. T., Pérez Chávez, J., Cargile, P. A., et al. 2021, [10.5281/zenodo.5131306](https://zenodo.org/record/5131306)
- Fűrész, G., Szentgyorgyi, A. H., & Meibom, S. 2008, **287**
- Foreman-Mackey, D., Czekala, I., Luger, R., et al. 2020, *exoplanet-dev/exoplanet* v0.2.6
- Fuhrmeister, B., Schmitt, J. H. M. M., & Hauschildt, P. H. 2005, *A&A*, **439**, 1137
- Fulton, B. J., Petigura, E. A., Howard, A. W., et al. 2017, *AJ*, **154**, 109
- Gagné, J., David, T. J., Mamajek, E. E., et al. 2020, *ApJ*, **903**, 96
- Gagné, J., Faherty, J. K., Moranta, L., & Popinchalk, M. 2021, [arXiv:2106.11873 \[astro-ph\]](https://arxiv.org/abs/2106.11873), arXiv: 2106.11873
- Gaia Collaboration, Babusiaux, C., van Leeuwen, F., et al. 2018a, *A&A*, **616**, A10
- Gaia Collaboration, Brown, A. G. A., Vallenari, A., et al. 2018b, *A&A*, **616**, A1
- . 2021a, *A&A*, **649**, A1
- Gaia Collaboration, Smart, R. L., Sarro, L. M., et al. 2021b, *A&A*, **649**, A6
- Gelman, A., & Rubin, D. B. 1992, *Statistical Science*, **7**, 457, publisher: Institute of Mathematical Statistics
- Gilbert, E. A., Barclay, T., Quintana, E. V., et al. 2022, *AJ*, **163**, 147
- Ginsburg, A., Sipocz, B., Madhura Parikh, et al. 2018, *Astropy/Astroquery: V0.3.7 Release*
- Ginzburg, S., Schlichting, H. E., & Sari, R. 2018, *MNRAS*, **476**, 759
- Girardi, L., Groenewegen, M. A. T., Hatziminaoglou, E., & da Costa, L. 2005, *A&A*, **436**, 895
- Goldberg, M., & Batygin, K. 2022, [arXiv:2203.00801 \[astro-ph\]](https://arxiv.org/abs/2203.00801), arXiv: 2203.00801
- Hattori, S., Foreman-Mackey, D., Hogg, D. W., et al. 2021, *arXiv e-prints*, arXiv:2106.15063
- Hawkins, K., Lucey, M., & Curtis, J. 2020, *MNRAS*, **496**, 2422
- Hedges, C., Hughes, A., Zhou, G., et al. 2021, *AJ*, **162**, 54
- Hoffman, M. D., & Gelman, A. 2014, *Journal of Machine Learning Research*, **15**, 1593
- Howard, A. W., Johnson, J. A., Marcy, G. W., et al. 2010, *ApJ*, **721**, 1467
- Jerabkova, T., Boffin, H. M. J., Beccari, G., et al. 2021, *a*, **647**, A137
- Jones, B. F., Shetrone, M., Fischer, D., & Soderblom, D. R. 1996, *AJ*, **112**, 186

- Jones, E., Oliphant, T., Peterson, P., et al. 2001, Open source scientific tools for Python
- Kerr, R. M. P., Rizzuto, A. C., Kraus, A. L., & Offner, S. S. R. 2021, *ApJ*, **917**, 23, aDS Bibcode: 2021ApJ...917...23K
- Kipping, D. M. 2013, *MNRAS*, **435**, 2152
- Kolbl, R., Marcy, G. W., Isaacson, H., & Howard, A. W. 2015, *AJ*, **149**, 18, aDS Bibcode: 2015AJ....149...18K
- Kounkel, M., & Covey, K. 2019, *AJ*, **158**, 122
- Kraus, A. L., Ireland, M. J., Huber, D., Mann, A. W., & Dupuy, T. J. 2016, *AJ*, **152**, 8
- Kraus, A. L., Shkolnik, E. L., Allers, K. N., & Liu, M. C. 2014, *AJ*, **147**, 146
- Krumholz, M. R., McKee, C. F., & Bland-Hawthorn, J. 2019, *ARA&A*, **57**, 227
- Lallement, R., Babusiaux, C., Vergely, J. L., et al. 2019, *a*, **625**, A135
- Lallement, R., Capitanio, L., Ruiz-Dern, L., et al. 2018, *A&A*, **616**, A132
- Lee, E. J., & Connors, N. J. 2021, *ApJ*, **908**, 32, aDS Bibcode: 2021ApJ...908...32L
- Lopez, E. D., Fortney, J. J., & Miller, N. 2012, *ApJ*, **761**, 59
- Luger, R., Agol, E., Foreman-Mackey, D., et al. 2019, *AJ*, **157**, 64
- Mann, A. W., Newton, E. R., Rizzuto, A. C., et al. 2016, *AJ*, **152**, 61
- Mann, A. W., Gaidos, E., Vanderburg, A., et al. 2017, *AJ*, **153**, 64
- Martioli, E., Hébrard, G., Correia, A. C. M., Laskar, J., & Lecavelier des Etangs, A. 2021, *A&A*, **649**, A177
- McInnes, L., Healy, J., & Astels, S. 2017, *The Journal of Open Source Software*, **2**, 205
- Meingast, S., Alves, J., & Fürnkranz, V. 2019, *A&A*, **622**, L13
- Meingast, S., Alves, J., & Rottensteiner, A. 2021, *A&A*, **645**, A84
- Messina, S., Lanzafame, A. C., Feiden, G. A., et al. 2016, *a*, **596**, A29
- Morris, R. L., Twicken, J. D., Smith, J. C., et al. 2017, Kepler Data Processing Handbook: Photometric Analysis, Kepler Science Document KSCI-19081-002
- Morton, T. D. 2012, *ApJ*, **761**, 6
- Morton, T. D. 2015, VESPA: False positive probabilities calculator, Astrophysics Source Code Library, [ascl:1503.011](#)
- Morton, T. D., Bryson, S. T., Coughlin, J. L., et al. 2016, *ApJ*, **822**, 86
- Nardiello, D., Piotto, G., Deleuil, M., et al. 2020, *MNRAS*, **495**, 4924
- Newton, E. R., Mann, A. W., Tofflemire, B. M., et al. 2019, *ApJ*, **880**, L17
- Owen, J. E., & Wu, Y. 2013, *ApJ*, **775**, 105
- Pecaut, M. J., & Mamajek, E. E. 2016, *MNRAS*, **461**, 794
- Petigura, E. A., Howard, A. W., Marcy, G. W., et al. 2017, *AJ*, **154**, 107, aDS Bibcode: 2017AJ....154..107P
- Plavchan, P., Barclay, T., Gagné, J., et al. 2020, *Nature*, **582**, 497
- Raghavan, D., McAlister, H. A., Henry, T. J., et al. 2010, *ApJS*, **190**, 1
- Randich, S., Tognelli, E., Jackson, R., et al. 2018, *A&A*, **612**, A99
- Rebull, L. M., Stauffer, J. R., Cody, A. M., et al. 2020 —, 2018, *AJ*, **155**, 196
- Rebull, L. M., Stauffer, J. R., Bouvier, J., et al. 2016, *AJ*, **152**, 113
- Ricker, G. R., Winn, J. N., Vanderspek, R., et al. 2015, *JATIS*, **1**, 014003
- Rizzuto, A. C., Newton, E. R., Mann, A. W., et al. 2020, *AJ*, **160**, 33
- Röser, S., Schilbach, E., & Goldman, B. 2016, *a*, **595**, A22
- Salvatier, J., Wiecki, T. V., & Fonnesbeck, C. 2016, PyMC3: Python probabilistic programming framework
- Schönrich, R., Binney, J., & Dehnen, W. 2010, *MNRAS*, **403**, 1829
- Short, C. I., & Doyle, J. G. 1998, *a*, **336**, 613
- Skumanich, A. 1972, *ApJ*, **171**, 565
- Smith, J. C., Morris, R. L., Jenkins, J. M., et al. 2016, *PASP*, **128**, 124501
- Smith, J. C., Stumpe, M. C., Jenkins, J. M., et al. 2017, *Kepler Science Document*, **8**
- Soderblom, D. R., Jones, B. F., Balachandran, S., et al. 1993, *AJ*, **106**, 1059
- Stauffer, J. R., Hartmann, L. W., Prosser, C. F., et al. 1997, *ApJ*, **479**, 776
- Stephenson, C. B. 1959, *PASP*, **71**, 145
- Theano Development Team. 2016, *arXiv e-prints*, [abs/1605.02688](#)
- Thompson, S. E., Coughlin, J. L., Hoffman, K., et al. 2018, *ApJS*, **235**, 38
- Tofflemire, B. M., Rizzuto, A. C., Newton, E. R., et al. 2021, *AJ*, **161**, 171
- Vogt, S. S., Allen, S. L., Bigelow, B. C., et al. 1994, SPIE Conference Series, ed. D. L. Crawford & E. R. Craine, Vol. 2198
- Yee, S. W., Petigura, E. A., & von Braun, K. 2017, *ApJ*, **836**, 77
- Zari, E., Hashemi, H., Brown, A. G. A., Jardine, K., & de Zeeuw, P. T. 2018, *A&A*, **620**, A172
- Zhou, G., Quinn, S. N., Irwin, J., et al. 2021, *AJ*, **161**, 2

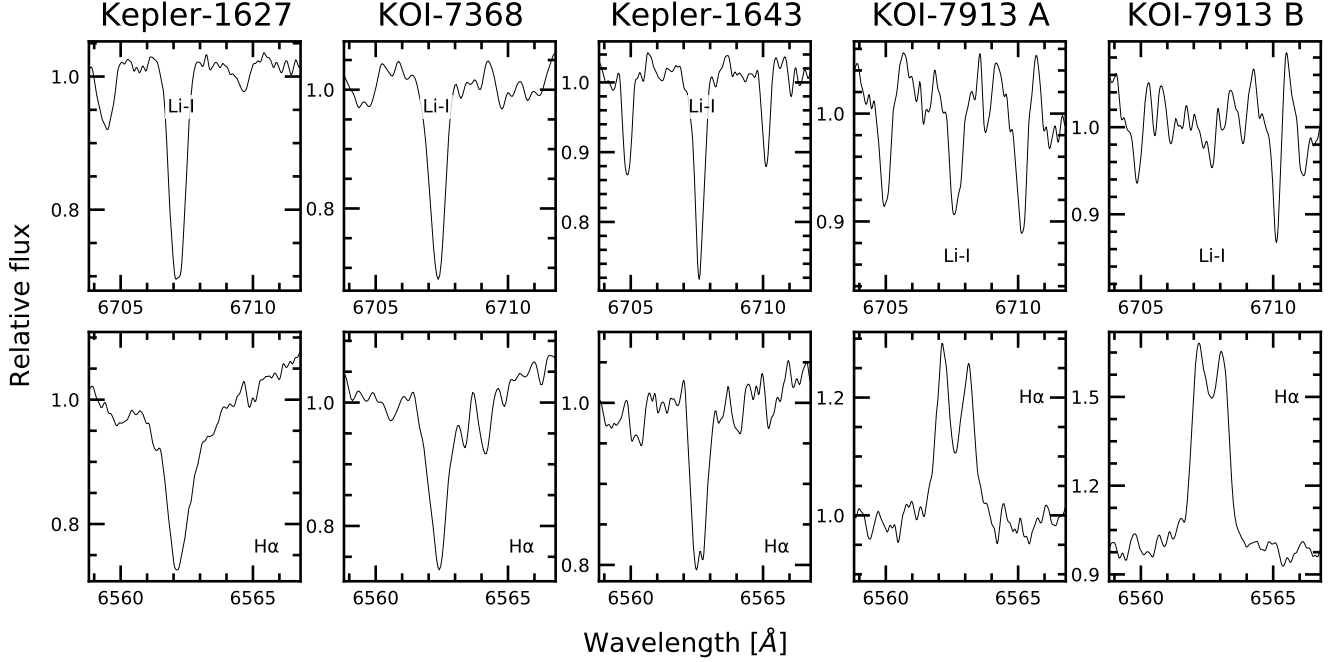


Figure 5. Spectroscopic youth diagnostics for Kepler-1627, KOI-7368, Kepler-1643, and KOI-7913 AB. The spectra are shown in the observed frame, and the stars are sorted left-to-right in order of decreasing effective temperature.

APPENDIX

A. TABLE OF CANDIDATE RSG-5 AND CH-2 MEMBERS

LGB TODO: add Gaia source lists and abbreviated info. Include rotation periods.

We measured rotation periods for 53 stars with ZTF and 51 stars with TESS, for a total of 71 periods reported for unique stars and 32 overlapping between the surveys. We adopted the ZTF period over the TESS period in three cases: (1) Gaia EDR3 2081755809272821248: the Lomb-Scargle periodogram favored 6.67 days, consistent with the ZTF period of 6.61 days; however, we flagged it as a candidate double-dipper, which appears to have inaccurately doubled the TESS period to 13.34 days; (2) Gaia EDR3 2081737529891330560: we found 3.06 days with TESS and 6.64 days with ZTF; we suspect that TESS captured the 1/2-period harmonic and adopt the approximately double value from ZTF; (3) 2134851775526125696: for this star, we measured 1.91 days with TESS from Cycle 2, but noted that the signal appeared to be missing in Cycle 4; ZTF found a strong signal at 12.23 days and we adopt this as the star’s period. In the remaining overlap cases, we adopted the average between TESS and ZTF as the final period. For these overlap stars, the median absolute deviation is 0.01 days, showing remarkable consistency between the surveys. For three stars, we failed to detect a period in TESS but recovered one from ZTF; in all cases the periods appear to be 13–16 days, pushing the limit of what is detectable with TESS with our procedure: (1) Gaia EDR3 2129930258400157440, TESS showed a flat light curve while ZTF yielded a 15.3-day period; (2) Gaia EDR3 2082376861542398336, LS found a 7.6-day period which we rejected during visual validation; we found 15.4 days with ZTF, and we suspect that the weak/rejected signal from TESS might have been a 1/2 period harmonic; (3) Gaia EDR3 2082397099429013120, similar to the previous case, we rejected a 6.7-day signal from TESS and recovered a 12.8-day period with ZTF.

B. SPECTROSCOPIC YOUTH INDICATORS

Figure 5 shows key portions of the HIRES and TRES spectra for the Kepler objects in Cep-Her. Lithium absorption is obvious at 6708Å in all stars except KOI-7913 B, where it is marginal. H α is in emission for both components of KOI-7913, and in absorption for the hotter stars. In the following, we compare these observations against stars in benchmark open clusters.

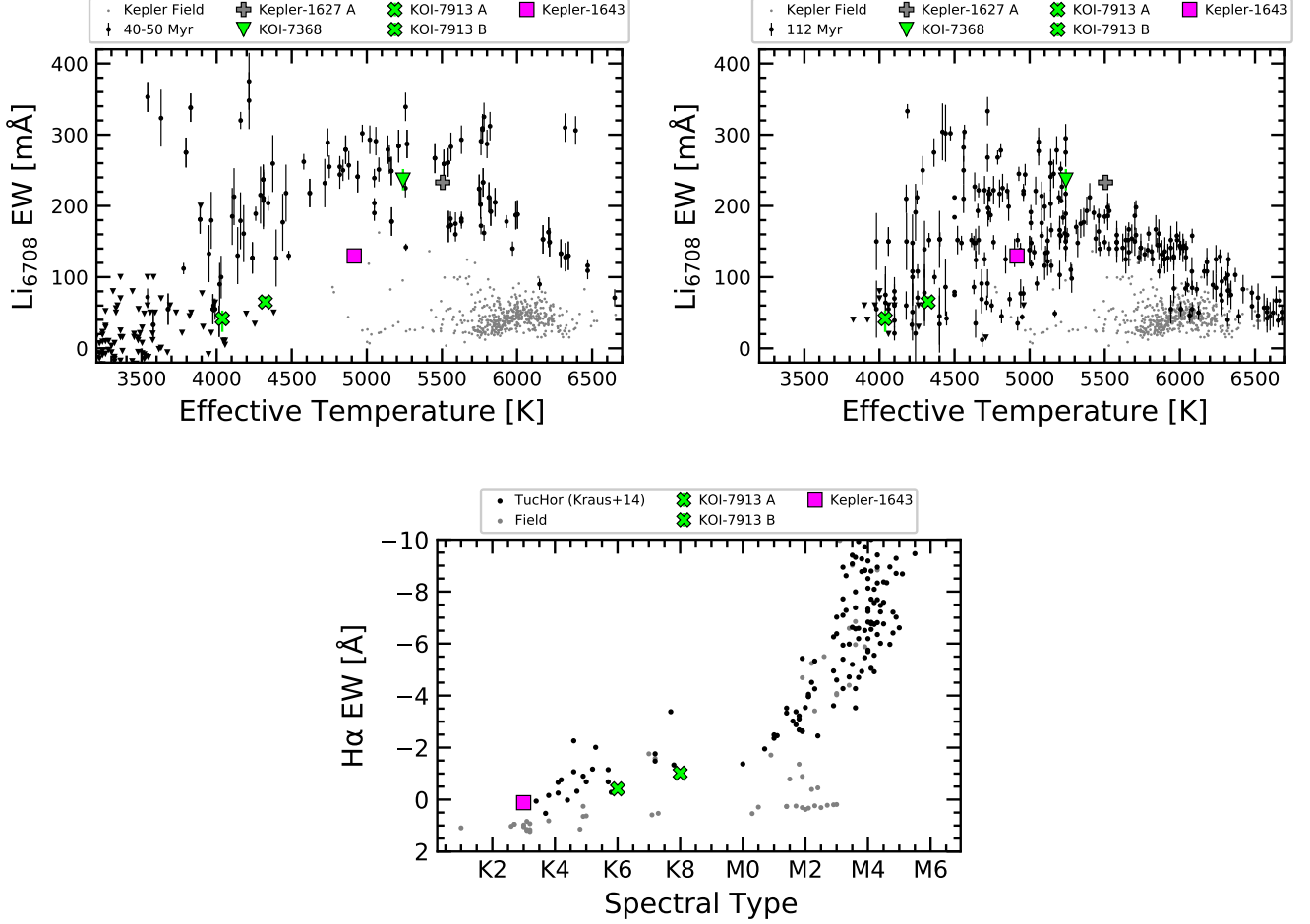


Figure 6. Lithium 6708 Å and H α equivalent widths for the objects of interest compared to young open clusters and field stars. Positive equivalent width means absorption; negative equivalent width means emission. The statistical uncertainties on the newly measured equivalent widths are shown, or else are smaller than the markers. *Top:* The field stars are stars with Kepler planets from [Berger et al. \(2018\)](#). The “40-50 Myr” reference stars (left) are from IC 2602 ([Randich et al. 2018](#)) and Tuc-Hor ([Kraus et al. 2014](#)). The “112 Myr” stars (right) are from the Pleiades ([Soderblom et al. 1993](#); [Jones et al. 1996](#); [Bouvier et al. 2018](#)). *Bottom:* The H α comparison is against Tuc-Hor (≈ 40 Myr; [Kraus et al. 2014](#))

B.1. Lithium

Figure 6 compares the measured lithium equivalent widths of the Kepler objects against a few reference populations. We selected studies from the literature only where upper limits were explicitly reported. KOI-7368 and KOI-7913 A have secure lithium detections, and the KOI-7913 B detection is marginal ($EW_{\text{Li}} = 42^{+12}_{-19}$). For all three stars, as well as for Kepler-1627 A, the observed lithium equivalent width is consistent with the stellar effective temperatures and ≈ 40 Myr ages.

Kepler-1643, in RSG-5, is conspicuously below the 40-50 Myr sequence in the left-panel of Figure 6, while still being above the field stars ($EW_{\text{Li}} = 130^{+6}_{-5}$). The right panel shows the comparison against the Pleiades, where Kepler-1643 is more consistent with the observed dispersion in lithium.

One explanation for this could be that Kepler-1643 is a field interloper; another could be that RSG-5 is older than 50 Myr. We do not favor the former, given that *i)* the star was selected based on its spatio-kinematic proximity to other RSG-5 members, nearly all of which appear consistent with being ≈ 50 Myr old (Figure 2 upper left), and *ii)* the same RSG-5 members display a gyrochronal sequence consistent with being younger than the Pleiades (Figure 2 lower left). We do not have an explanation, but in the following paragraph speculate on one possible line of future work that might help resolve the discrepancy.

Analyzing Figure 6, it is remarkable that in just 50 million years, stars between 4500 K and 5200 K go from having such a tight lithium sequence to one with a dispersion $\approx 10\times$ greater. The existence of such a dispersion in Pleiades-age K-dwarfs has been

known for longer than some of the present authors have been alive; it has also been known that the stars with the most lithium are also the most rapidly rotating (Butler et al. 1987; Soderblom et al. 1993). More recent analyses of this correlation have been reviewed by Bouvier (2020). The conclusion of that work was that the origin of the rotation-lithium correlation likely lies within pre-main-sequence stellar physics. If so, one would expect the IC 2062 and Tuc-Hor K-dwarfs to show a larger intrinsic lithium dispersion, which they do not. It seems therefore that the exact onset time of the K-dwarf lithium dispersion might be worth clarifying. Messina et al. (2016) for instance do not obviously see it in the β Pic moving group (25 ± 3 Myr). Given that RSG-5 seems somewhat isochronally older than the δ Lyr cluster (and therefore IC 2602 Bouma et al. 2022), it might be a worthy cluster for such an analysis.

B.2. $H\alpha$

As shown in Figure 5, $H\alpha$ is in emission for both components of KOI-7913, and in absorption for the hotter stars. Additionally, the emission appears double-peaked for both of the KOI-7913 components. We note that KOI-7913 A and KOI-7913 B were spatially resolved from each other during data acquisition. Performing a cross-correlation between each of the stars and the nearest matches in the Keck/HIRES template library, we also found that the CCFs for both components of KOI-7913 showed no indications of double-lined binarity (Kolbl et al. 2015).

Balmer line emission, particularly for $H\alpha$, is expected for stars of this age. Kraus et al. (2014) for instance, in their survey of Tuc-Hor (≈ 40 Myr), observed that essentially all cluster members with spectral type $> K4.5V$ had $H\alpha$ in emission. This agrees with our observations that KOI-7913 shows $H\alpha$ in emission for both components, while it is in absorption for all of our other Kepler objects. The double-peaked nature of the emission, though not always present, is also not particularly rare for active stars. Proxima Centauri, for instance, has double-peaked $H\alpha$ emission (Collins et al. 2017). A simple explanation is self-absorption: photons nearest the center of the line see a greater optical depth from higher layers of the chromosphere, while photons on the wings are on average too far from the rest-wavelength to excite electrons and be re-absorbed in the upper layers. The exact details of when a star’s atmosphere reaches the conditions for such self-absorption require non-local thermal equilibrium models of the chromosphere (Short & Doyle 1998; Fuhrmeister et al. 2005).

C. TABLE OF TRANSIT FIT PARAMETERS

Tables 1, 2, 3 give the full set of fitted and derived parameters from the model described in Section 4.2. Priors and convergence statistics are also listed.

D. DISPOSITION HISTORY OF KOI-7913

The disposition of KOI-7913.01 has been debated: in `q1_q17_dr25_koi` the source was flagged as a false positive, with the comment “cent_kic_pos—halo_ghost”. This comment and disposition were removed in the `q1_q17_dr25_sup_koi` data release, which renamed the planet a “candidate”. In this note, we discuss the interpretation of these flags (which do not apply to the system, according to the latest analysis). We also discuss how the relative locations of KOI-7913 A and KOI-7913 B affect the interpretation of the Kepler data.

As described by Thompson et al. (2018), the “cent_kic_pos” flag is an indication that the measured source centroid is offset from its expected location in the Kepler Input Catalog. The final Kepler data validation reports, generated 2016 Jan 30, do not show this to be the case for KOI-7913. Moreover, the statistical significance of any centroid offset is lower than for KOI-7368 and Kepler-1643 (which both show centroid offsets that are likely explained by the stellar variability).

What of the “halo_ghost” flag? This test measures the transit strength for the pixels inside the aperture, and compares it to that measured in the ring of pixels around said aperture (the “halo”). Generally one expects the transit signal to be strongest in the central aperture, rather than the halo. Two types of false positive scenarios can change this and trigger the flag: the first is when optical ghosts from bright eclipsing binaries reflect off the CCD, and contaminate the target star. The second is when the PRF of nearby stars directly overlaps with the PRF of the target star (see Thompson et al. 2018, Section A.5.2). The most obvious explanation for KOI-7913 is the latter case, given that KOI-7913 B is ≈ 0.9 Kepler pixels away from Kepler-7913 A and so it usually part of the “halo”. Due to the on-sky orientation of KOI-7913 A and KOI-7913 B, the default “optimal aperture” selected in quarters 3, 7, 11, and 15 in fact included both stars, while for the remaining quarters KOI-7913 B was excluded from the optimal aperture but was included as part of the halo (see pages 35 through 71 of the data validation reports.)

Given the orientation of the stars and the ≈ 1.5 pixel FWHM of the Kepler pixel response function, some blending between the two stars is present. The pointing geometries from quarters 3, 7, 11, and 15 however did not noticeably affect the observed transit depths, which is an indication that the crowding metric applied in the data products accurately correct the mean flux level (Morris et al. 2017). Analysis of the target-pixel data that was acquired separately for KOI-7913 B also reveals a clearly different stellar rotation period, and no hint of the transit signal.

Table 1. Priors and posteriors for Kepler-1643 transit model with local polynomials removed.

Param.	Unit	Prior	Median	Mean	Std. Dev.	3% HDI	97% HDI	ESS	$\hat{R} - 1$
P	d	$\mathcal{N}(5.34264; 0.01000)$	5.3426257	5.3426258	0.0000101	5.3426071	5.3426454	7884	1.1e-03
$t_0^{(1)}$	d	$\mathcal{N}(134.38100; 0.02000)$	134.3820412	134.3820408	0.0011172	134.3798834	134.3840798	7390	3.7e-04
$\log R_p/R_*$	—	$\mathcal{U}(-6.215; 0.000)$	-3.68806	-3.68934	0.02072	-3.72788	-3.65275	4449	-7.8e-05
b	—	$\mathcal{U}(0; 1 + R_p/R_*)$	0.5825	0.5781	0.0514	0.4848	0.6734	4705	1.9e-04
u_1	—	Kipping 2013	0.257	0.294	0.214	0.000	0.678	5324	7.9e-04
u_2	—	Kipping 2013	0.324	0.314	0.324	-0.257	0.880	4908	8.4e-04
R_*	R_\odot	$\mathcal{N}(0.855; 0.044)$	0.851	0.851	0.045	0.766	0.933	7473	7.2e-04
$\log g$	cgs	$\mathcal{N}(4.502; 0.035)$	4.507	4.507	0.035	4.442	4.576	6530	-1.4e-04
$\log \sigma_f$	—	$\mathcal{N}(\log \langle \sigma_f \rangle; 2.000)$	-8.520	-8.520	0.019	-8.556	-8.486	7966	2.1e-04
$\langle f \rangle$	—	$\mathcal{N}(1.000; 0.100)$	1.0000	1.0000	0.0000	1.0000	1.0000	7488	3.2e-04
R_p/R_*	—	—	0.025	0.025	0.001	0.024	0.026	4449	-7.8e-05
ρ_*	g cm^{-3}	—	1.943	1.953	0.191	1.603	2.313	6081	9.4e-05
R_p	R_{Jup}	—	0.207	0.207	0.012	0.184	0.231	6326	2.5e-04
R_p	R_{Earth}	—	2.32	2.32	0.135	2.062	2.589	6326	2.5e-04
a/R_*	—	—	14.312	14.322	0.465	13.487	15.228	6081	8.2e-05
$\cos i$	—	—	0.041	0.040	0.005	0.032	0.049	4929	2.4e-04
T_{14}	hr	—	2.408	2.409	0.061	2.304	2.527	4774	5.3e-04
T_{13}	hr	—	2.232	2.233	0.070	2.109	2.362	4561	6.2e-04

NOTE— ESS refers to the number of effective samples. \hat{R} is the Gelman-Rubin convergence diagnostic. Logarithms in this table are base- e . \mathcal{U} denotes a uniform distribution, and \mathcal{N} a normal distribution. Many of the T_{13} statistics may be nan in the event of a grazing transit. (1) The ephemeris is in units of BJKD (BJDTDB-2454833).

Table 2. Priors and posteriors for KOI-7368 transit model with local polynomials removed.

Param.	Unit	Prior	Median	Mean	Std. Dev.	3% HDI	97% HDI	ESS	$\hat{R} - 1$
P	d	$\mathcal{N}(6.84294; 0.01000)$	6.8430344	6.8430341	0.0000125	6.8430107	6.8430574	10045	6.5e-05
$t_0^{(1)}$	d	$\mathcal{N}(137.06000; 0.02000)$	137.0463023	137.0463315	0.0014043	137.0436532	137.0489229	10303	9.2e-05
$\log R_p/R_*$	—	$\mathcal{U}(-4.605; 0.000)$	-3.76025	-3.76299	0.03062	-3.81932	-3.70774	4043	6.3e-04
b	—	$\mathcal{U}(0; 1 + R_p/R_*)$	0.5077	0.4999	0.0641	0.3797	0.6115	4434	3.5e-04
u_1	—	Kipping 2013	0.976	0.953	0.267	0.425	1.422	5809	-5.6e-05
u_2	—	Kipping 2013	-0.191	-0.158	0.308	-0.661	0.421	4387	2.6e-04
R_*	R_\odot	$\mathcal{N}(0.876; 0.035)$	0.874	0.874	0.036	0.804	0.938	9902	7.3e-04
$\log g$	cgs	$\mathcal{N}(4.499; 0.030)$	4.503	4.502	0.030	4.445	4.557	7527	2.7e-05
$\log \sigma_f$	—	$\mathcal{N}(\log \langle \sigma_f \rangle; 2.000)$	-8.314	-8.314	0.012	-8.337	-8.292	10636	1.3e-03
$\langle f \rangle$	—	$\mathcal{N}(1.000; 0.100)$	1.0000	1.0000	0.0000	1.0000	1.0000	9742	-2.9e-04
R_p/R_*	—	—	0.023	0.023	0.001	0.022	0.025	4043	6.3e-04
ρ_*	g cm^{-3}	—	1.872	1.878	0.151	1.593	2.159	6829	3.4e-04
R_p	R_{Jup}	—	0.198	0.198	0.011	0.177	0.218	5676	2.8e-04
R_p	R_{Earth}	—	2.219	2.219	0.123	1.984	2.444	5676	2.8e-04
a/R_*	—	—	16.671	16.677	0.447	15.863	17.542	6829	3.3e-04
$\cos i$	—	—	0.030	0.030	0.004	0.022	0.038	4518	5.4e-04
T_{14}	hr	—	2.789	2.792	0.075	2.651	2.928	4845	5.0e-04
T_{13}	hr	—	2.619	2.622	0.085	2.470	2.779	4575	3.1e-04

NOTE— ESS refers to the number of effective samples. \hat{R} is the Gelman-Rubin convergence diagnostic. Logarithms in this table are base- e . \mathcal{U} denotes a uniform distribution, and \mathcal{N} a normal distribution. Many of the T_{13} statistics may be nan in the event of a grazing transit. (1) The ephemeris is in units of BJKD (BJDTDB-2454833).

Table 3. Priors and posteriors for KOI-7913 A transit model with local polynomials removed.

Param.	Unit	Prior	Median	Mean	Std. Dev.	3% HDI	97% HDI	ESS	$\hat{R} - 1$
P	d	$\mathcal{N}(24.27838; 0.01000)$	24.2785532	24.2785706	0.0002630	24.2781117	24.2790852	4413	1.5e-03
$t_0^{(1)}$	d	$\mathcal{N}(154.51300; 0.05000)$	154.5121202	154.5124405	0.0062825	154.4998424	154.5237474	5612	6.0e-04
$\log R_p/R_*$	—	$\mathcal{U}(-5.298; 0.000)$	-3.59884	-3.60184	0.04605	-3.68852	-3.51878	4290	5.6e-04
b	—	$\mathcal{U}(0; 1 + R_p/R_*)$	0.3120	0.2985	0.1526	0.0045	0.5232	2373	1.8e-03
u_1	—	Kipping 2013	0.267	0.337	0.281	0.000	0.862	4491	-6.1e-05
u_2	—	Kipping 2013	0.209	0.229	0.325	-0.309	0.860	5935	7.0e-04
R_*	R_\odot	$\mathcal{N}(0.790; 0.049)$	0.788	0.788	0.049	0.699	0.881	6847	2.8e-04
$\log g$	cgs	$\mathcal{N}(4.523; 0.043)$	4.526	4.527	0.042	4.450	4.606	5714	6.6e-04
$\log \sigma_f$	—	$\mathcal{N}(\log \langle \sigma_f \rangle; 2.000)$	-7.197	-7.197	0.019	-7.230	-7.161	6976	1.4e-04
$\langle f \rangle$	—	$\mathcal{N}(1.000; 0.100)$	1.0000	1.0000	0.0000	1.0000	1.0000	6998	2.8e-04
R_p/R_*	—	—	0.027	0.027	0.001	0.025	0.030	4290	5.6e-04
ρ_*	g cm^{-3}	—	2.199	2.213	0.250	1.781	2.705	5357	5.6e-04
R_p	R_{Jup}	—	0.209	0.209	0.016	0.179	0.238	4882	1.3e-03
R_p	R_{Earth}	—	2.343	2.343	0.179	2.006	2.668	4882	1.3e-03
a/R_*	—	—	40.920	40.949	1.539	38.143	43.845	5357	6.6e-04
$\cos i$	—	—	0.008	0.007	0.004	0.000	0.013	2344	1.9e-03
T_{14}	hr	—	4.394	4.396	0.207	3.980	4.758	3952	5.6e-04
T_{13}	hr	—	4.133	4.132	0.222	3.715	4.548	3632	7.6e-04

NOTE—ESS refers to the number of effective samples. \hat{R} is the Gelman-Rubin convergence diagnostic. Logarithms in this table are base- e . \mathcal{U} denotes a uniform distribution, and \mathcal{N} a normal distribution. Many of the T_{13} statistics may be nan in the event of a grazing transit. (1) The ephemeris is in units of BJKD (BJDTDB-2454833).